

Modelling and simulation of electromechanically coupled dielectric elastomers and myocardial tissue using smoothed finite element methods

Tan Tran^a, Denisa Martonová^b, and Sigrid Leyendecker^a

^a*Friedrich-Alexander-Universität Erlangen-Nürnberg, Institute of Applied Dynamics, Immwahrstraße 1, 91058 Erlangen, Germany*

^b*Friedrich-Alexander-Universität Erlangen-Nürnberg, Institute of Applied Mechanics, Egerlandstraße 5, 91058 Erlangen, Germany*

Abstract

Computational modelling offers a cost-effective and time-efficient alternative to experimental studies in biomedical engineering. In cardiac electromechanics, finite element method-based simulations provide valuable insights into diseased tissue behaviour and the development of assistive systems often employing dielectric elastomer actuators (DEAs). However, the use of automatically generated tetrahedral meshes, commonly applied due to geometric complexity of the computational domain, often leads to numerical issues including overly stiff responses and volume locking, particularly in incompressible materials. Smoothed finite element methods (S-FEMs) offer a promising alternative by softening the stiffness matrix through gradient smoothing over defined smoothing domains. This work extends S-FEM formulations to electromechanically coupled problems and compares their performance against standard FEM. We implement and evaluate four approaches in the Abaqus environment through custom user elements: Standard TET-FEM, face-based S-FEM (FS-FEM), node-based S-FEM (NS-FEM), and the hybrid face/node-based S-FEM (FSNS-FEM). Two benchmark problems for nearly incompressible materials are studied: The electrically induced contraction of an isotropic cube representing a simplified DEA and an anisotropic cube representing a section of the myocardium. Reference solutions are obtained using a higher-order method. Our results demonstrate that FSNS-FEM provides the best balance between accuracy and computational efficiency, closely matching reference data. NS-FEM produces softer results, which is beneficial for anisotropic materials such as the myocardium but less accurate for isotropic elastomers. FS-FEM and standard FEM consistently exhibit overly stiff behaviour, with pronounced volume locking in the myocardial case. These findings support the potential of S-FEMs, in particular FSNS-FEM, for accurate simulation of coupled electromechanical behaviour in complex biomedical applications.

keywords: smoothed finite element method; electromechanical coupling; dielectric elastomer; myocardium; cardiac tissue; volumetric locking; incompressible material; Abaqus

1 Introduction

Cardiovascular diseases (CVDs) represent the leading cause of death worldwide [World Health Organization, 2021]. CVDs comprise a broad spectrum of pathological conditions involving the heart and vascular system, with ischaemic heart disease and stroke being the most prevalent manifestations [Townsend et al., 2022]. At the core of cardiac function lies a coupled electromechanical process: An electrical signal propagates through the cardiac tissue, initiating the contraction of cardiac muscle cells, cardiomyocytes, which in turn drives the mechanical action of blood circulation. This coupling between electrical excitation and mechanical contraction, referred to as excitation-contraction coupling, is fundamental to the normal functioning of myocardial tissue. Accurately capturing this behaviour through computational modelling is essential for advancing our understanding of cardiac mechanics and electrophysiology, and for evaluating the behaviour of biologically inspired materials under coupled field conditions. The finite element method (FEM) is widely employed in the simulation of biological tissues because it can accommodate complex geometries, heterogeneous materials, and nonlinear deformation. Particularly in cardiac applications, tetrahedral (TET) meshes are favored due to their adaptability to intricate anatomical shapes, and can be efficiently generated through algorithms such as Delaunay triangulation. However, the use of linear TET elements in nearly incompressible soft tissue often leads to well-known numerical issues such as volumetric locking and overly stiff behaviour [Liu, 2019]. Remedies for these challenges include the use of higher-order elements or significantly refined meshes, both of which increase computational cost. An alternative approach is the smoothed finite element method (S-FEM), which combines aspects of mesh-free methods with conventional FEM techniques [Liu et al., 2007, Liu, 2019, Martonová et al., 2021, Martonová et al., 2023]. S-FEM improves solution accuracy and convergence properties without the need for mesh refinement or higher-order basis functions. In contrast to standard FEM, where strains and stresses are derived element-wise, S-FEM computes smoothed gradients over specifically defined smoothing domains (SDs), which are constructed based on the original mesh topology. Depending on the SD configuration, several S-FEM variants exist. For three-dimensional (3D) problems, commonly used schemes include face-based S-FEM (FS-FEM) introduced by [Nguyen-Thoi et al., 2009], node-based S-FEM (NS-FEM) introduced by [Liu et al., 2009], and hybrid schemes such as the face-node selective S-FEM (FSNS-FEM) proposed by [Jiang et al., 2014]. Previous studies have demonstrated the effectiveness of S-FEM for modelling large deformation of soft, anisotropic, and (nearly) incompressible materials, including biological tissues. For instance, FS-FEM has been applied to hyperelastic tissue modelling [Minh Tuan Duong, 2014] and mechanical simulations of soft organs [Mendizabal et al., 2017]. FSNS-FEM and edge-node schemes

have also been implemented in models of passive myocardium with complex fibre orientations [Jiang et al., 2014, Jiang et al., 2015]. Further, different S-FEM techniques have been used in simulation of active cardiac mechanics modelled with a time-dependent, rather than potential-dependent, active stress [Martonová et al., 2021, Martonová et al., 2023]. In summary, all of these applications treat solely the mechanical problem via S-FEM, without accounting for the coupling between electrical and mechanical quantities in the smoothing domains. Recently, S-FEM has been successfully extended to electromechanical coupling, but only so far in piezoelectric contexts using cell-based smoothing domains [Cai and Zhou, 2019, Zheng et al., 2019]. While several finite element formulations exist for electromechanically coupled dielectric elastomers [Henann et al., 2013, Wang et al., 2016] and cardiac tissue [Göktepe and Kuhl, 2010, Martonová et al., 2023], these methods predominantly rely on standard FEM discretisations. To date, no work has demonstrated the application of S-FEMs to such coupled problems involving dielectric elastomers or cardiac tissue and a systematic comparison across different S-FEM variants in this context remains unexplored. This highlights a research gap and provides the motivation for the current study. The goal of this work is to develop and evaluate S-FEM-based formulations for modelling electromechanically coupled problems in soft dielectric and biological materials. Specifically, we develop various electromechanically coupled S-FEMs, including FS-FEM, NS-FEM, and FSNS-FEM using linear TET meshes, and compare their performance against standard TET-FEM. The study focuses on both numerical accuracy and computational efficiency in the context of large-deformation simulations. This paper is organised as follows: First, we introduce the continuum mechanics framework, including the strong and weak forms of the governing electromechanical equations. Second, we present the constitutive models for hyperelastic, nearly incompressible dielectric elastomers and incompressible myocardial tissue. Third, we outline the numerical solution strategy, describe the integration of S-FEM into the iterative finite element solver, and summarize implementation details. Finally, two benchmark problems are simulated: an electro-active dielectric elastomer cube representing a simplified DEA and a cubic myocardial segment. Results are compared across the FEM and S-FEM schemes to assess differences in solution quality and computational cost.

2 Coupled problem formulation

In this section, we state the fundamental equations and continuum mechanical framework to describe the electromechanically coupled problem for the dielectric elastomer and the myocardial tissue. First, we introduce fundamental kinematic quantities to describe the large deformation of soft material. Then, the partial differential equations (PDEs) are stated for the electrical polarisation and mechanical deformation. To later apply the nu-

merical methods, we also introduce the weak forms of the governing PDEs.

2.1 Kinematics of large deformations

To describe large deformations, we introduce fundamental quantities based on the finite strain theory which is part of non-linear continuum mechanics. For further information regarding the formulas and theorems, the reader is referred to [Bonet and Wood, 1997, Wriggers, 2008].

Let us first consider an undeformed body in the material configuration \mathcal{B}_0 . Points inside \mathcal{B}_0 are described by material coordinates $\mathbf{X} = \mathbf{X}(t_0)$ for a given initial time t_0 . The deformed body is set in the spatial configuration \mathcal{B} where the position of a point is described by the corresponding spatial coordinates $\mathbf{x} = \mathbf{x}(\mathbf{X}, t)$ at a certain time $t \geq t_0$. The spatial coordinates represent unique and continuous differential mappings of the material coordinates from \mathcal{B}_0 to \mathcal{B} with

$$\mathbf{x} : \mathcal{B}_0 \rightarrow \mathcal{B}, \quad \mathbf{X} \mapsto \mathbf{x}(\mathbf{X}, t) \quad (1)$$

which is known as the Lagrangian description of motion. Both material and spatial coordinates share the same basis. The displacement \mathbf{u} is defined as the difference between the spatial and the material coordinates with

$$\mathbf{u}(\mathbf{X}, t) = \mathbf{x}(\mathbf{X}, t) - \mathbf{X}. \quad (2)$$

In non-linear continuum mechanics, the deformation gradient \mathbf{F} is necessary to map tangents between \mathcal{B}_0 and \mathcal{B} . It is a second order tensor which is computed using the gradient of the deformation mapping with respect to the material coordinates

$$\mathbf{F} = \frac{\partial \mathbf{x}}{\partial \mathbf{X}} = \frac{\partial (\mathbf{u} + \mathbf{X})}{\partial \mathbf{X}} = \frac{\partial \mathbf{u}}{\partial \mathbf{X}} + \mathbf{I} \quad (3)$$

where \mathbf{I} denotes the second-order identity tensor. The determinant of the deformation gradient is denoted as the Jacobian $J = \det(\mathbf{F})$ and is relevant to describe the volume change during the deformation. The general deformation mapping in non-linear kinematics is illustrated in Figure 1. There, \mathbf{E}_i denote the material basis vectors and \mathbf{e}_i denote the spatial basis vectors. The following formulas describe the transformation of line, area and volume elements from \mathcal{B}_0 to \mathcal{B}

$$d\mathbf{x} = \mathbf{F}d\mathbf{X}, \quad (4a)$$

$$\mathbf{n}da = J\mathbf{F}^{-T} \cdot \mathbf{N}dA \text{ and} \quad (4b)$$

$$dv = JdV \quad (4c)$$

where \mathbf{N} and \mathbf{n} denote the outward unit normal vectors in \mathcal{B}_0 and \mathcal{B} respectively. The existence of \mathbf{F}^{-T} implies that J must be non-zero. Also, the transformation of the volume elements demands J to be non-negative and

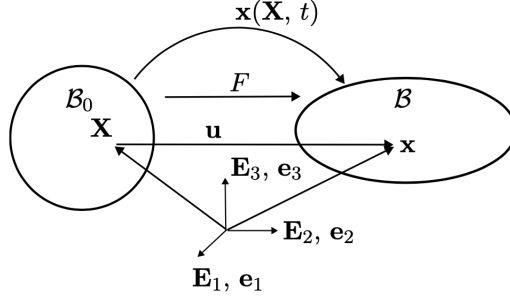


Figure 1: Deformation mapping from the undeformed body \mathcal{B}_0 to the deformed body \mathcal{B} .

therefore $J > 0$. To describe the non-linear deformation, we utilize different strain measurements. To account for the geometrical change from \mathcal{B}_0 to \mathcal{B} , the right Cauchy-Green tensor $\mathbf{C} = \mathbf{F}^T \mathbf{F}$ is used. Respectively, the left Cauchy-Green tensor $\mathbf{b} = \mathbf{F} \mathbf{F}^T$ is used to describe the geometrical change from \mathcal{B} to \mathcal{B}_0 . In particular, for nearly incompressible materials, it is useful to separate the deformation into a volumetric and isochoric part where the latter does not result in any volume change. The isochoric component $\bar{\mathbf{F}}$ of \mathbf{F} is defined as

$$\bar{\mathbf{F}} = J^{-\frac{1}{3}} \mathbf{F}. \quad (5)$$

It is evident that $\det(\bar{\mathbf{F}}) = 1$ meaning that there is no volume change. Using the decomposition of \mathbf{F} , the isochoric parts of \mathbf{C} and \mathbf{b} are obtained as

$$\bar{\mathbf{C}} = \bar{\mathbf{F}}^T \bar{\mathbf{F}} = J^{-\frac{2}{3}} \mathbf{C} \text{ and } \bar{\mathbf{b}} = \bar{\mathbf{F}} \bar{\mathbf{F}}^T = J^{-\frac{2}{3}} \mathbf{b}. \quad (6)$$

2.2 Governing equations of electromechanics

We now introduce the necessary PDEs to model the electromechanically coupled behaviour. Additionally, essential boundary conditions are defined to complete the strong problem formulation.

The mechanical deformation of a body is described by the balance of linear momentum with prescribed Dirichlet and Neumann boundary conditions. Neglecting body forces and inertia forces, the following mechanical boundary value problem (BVP) results

$$\operatorname{div}(\boldsymbol{\sigma}) = \mathbf{0} \text{ in } \mathcal{B} \quad (7a)$$

$$\mathbf{u} = \bar{\mathbf{u}} \text{ on } \mathcal{S}_{\mathbf{u}} \quad (7b)$$

$$\boldsymbol{\sigma} \mathbf{n} = \bar{\mathbf{t}} \text{ on } \mathcal{S}_{\mathbf{t}}. \quad (7c)$$

In (7), the Cauchy stress is denoted as $\boldsymbol{\sigma}$. Regarding the boundary conditions, the displacement $\bar{\mathbf{u}}$ and the surface traction force $\bar{\mathbf{t}}$ are prescribed on the complementary boundary domains $\mathcal{S}_{\mathbf{u}}$ and $\mathcal{S}_{\mathbf{t}}$ with $\mathcal{S}_{\mathbf{u}} \cup \mathcal{S}_{\mathbf{t}} = \partial \mathcal{B}$ and

$$\mathcal{S}_u \cap \mathcal{S}_t = \emptyset.$$

Neglecting magnetic effects, the spatial propagation of the electric potential φ inside a dielectric elastomer is described by Maxwell's first equation. We adopt the electric BVP for a dielectric elastomer from [Henann et al., 2013] with prescribed boundary conditions as

$$\operatorname{div}(\mathbf{D}) = 0 \text{ in } \mathcal{B} \quad (8a)$$

$$\varphi = \bar{\varphi} \text{ on } \mathcal{S}_\varphi \quad (8b)$$

$$-\mathbf{D}\mathbf{n} = \bar{\omega} \text{ on } \mathcal{S}_\omega. \quad (8c)$$

In (8), the spatial electric displacement is denoted as \mathbf{D} . Regarding the boundary conditions, the electric potential $\bar{\varphi}$ and the surface charge $\bar{\omega}$ are prescribed on the complementary boundary domains \mathcal{S}_φ and \mathcal{S}_ω with $\mathcal{S}_\varphi \cup \mathcal{S}_\omega = \partial\mathcal{B}$ and $\mathcal{S}_\varphi \cap \mathcal{S}_\omega = \emptyset$.

For the electrical behaviour of the myocardial tissue, we adopt the model stated in [Göktepe and Kuhl, 2009]. The spatio-temporal evolution of φ inside the myocardium is defined by the following initial BVP

$$\dot{\varphi} = \operatorname{div}(\mathbf{q}) + I^\varphi \text{ in } \mathcal{B} \cup [t_0, \infty) \quad (9a)$$

$$\varphi_0 = \varphi(t_0) \text{ in } \mathcal{B} \cup \{t_0\} \quad (9b)$$

$$\varphi = \bar{\varphi} \text{ on } \mathcal{S}_\varphi \cup [t_0, \infty) \quad (9c)$$

$$\mathbf{q}\mathbf{n} = \bar{q} \text{ on } \mathcal{S}_q \cup [t_0, \infty). \quad (9d)$$

In (9), the diffusion term $\operatorname{div}(\mathbf{q})$ defines the spatial propagation of φ depending on the spatial flux vector \mathbf{q} . Additionally, the non-linear source term I^φ defines the generation and evolution of φ over time. For our work, it is computed based on the Aliev-Panfilov model introduced in [Aliev and Panfilov, 1996]. Regarding the boundary conditions, the electric potential $\bar{\varphi}$ and the surface flux \bar{q} are prescribed on the complementary boundary domains \mathcal{S}_φ and \mathcal{S}_q with $\mathcal{S}_\varphi \cup \mathcal{S}_q = \partial\mathcal{B}$ and $\mathcal{S}_\varphi \cap \mathcal{S}_q = \emptyset$.

In order to later apply the discretisation and numerical solution scheme, we rewrite the PDEs from above into a weak formulation. The Galerkin method is utilized to derive the weak forms of the PDEs from (7)-(9). Therefore, we introduce the following test functions \mathbf{v}_1 and v_2 and their respective sets \mathcal{V}_1 and \mathcal{V}_2 as follows

$$\mathcal{V}_1 = \{\mathbf{v}_1 \in \mathcal{H}^1 : \mathbf{v}_1 = \mathbf{0} \text{ on } \mathcal{S}_u\} \text{ and} \quad (10a)$$

$$\mathcal{V}_2 = \{v_2 \in \mathcal{H}^1 : v_2 = 0 \text{ on } \mathcal{S}_\varphi\} \quad (10b)$$

where \mathcal{H}^1 is the Sobolev-space. The test functions have the property that they vanish on the Dirichlet boundary domain. The spatial weak form for the mechanical problem in (7) is given by

$$\mathcal{G}_u(\mathbf{u}, \mathbf{v}_1) = - \int_{\mathcal{B}} \frac{\partial \mathbf{v}_1}{\partial \mathbf{x}} : \boldsymbol{\sigma} dv + \int_{\mathcal{S}_t} \mathbf{v}_1 \mathbf{t} da = 0, \quad \forall \mathbf{v}_1 \in \mathcal{V}_1. \quad (11)$$

The spatial weak form for the electrical dielectric elastomer problem from (8) is given by

$$\mathcal{G}_\varphi^{\text{die}}(\varphi, v_2) = \int_{\mathcal{B}} \frac{\partial v_2}{\partial \mathbf{x}} \mathbf{D} dv - \int_{\mathcal{S}_q} v_2 \bar{\omega} da = 0, \quad \forall v_2 \in \mathcal{V}_2. \quad (12)$$

Both formulations correspond to the weak forms stated in [Henann et al., 2013]. The spatial weak form for the electrical myocardial tissue problem from (9) is derived in [Göktepe and Kuhl, 2010] to

$$\mathcal{G}_\varphi^{\text{myo}}(\varphi, v_2) = \int_{\mathcal{B}} [v_2 \dot{\varphi} + \frac{\partial v_2}{\partial \mathbf{x}} \mathbf{q} - V_2 I^\varphi] dv - \int_{\mathcal{S}_q} v_2 \bar{q} da = 0, \quad \forall v_2 \in \mathcal{V}_2. \quad (13)$$

It can be shown that solutions of the strong formulations in (7)-(9) also satisfy the corresponding weak formulation in (11)-(13). The use of the weak formulations poses less continuity requirements on the solution making it suitable for the use in FEM.

3 Constitutive equations

In this section, we summarize the constitutive equations for the dielectric elastomer and the myocardial tissue. These equations relate the solution variables \mathbf{u}, φ to the stress and electrical quantities from (7) - (9) and therefore characterise the coupling behaviour.

3.1 Constitutive equations for the dielectric elastomer

Based on Gauss's law, \mathbf{D} from (8) is computed as

$$\mathbf{D} = \epsilon \mathbf{E}. \quad (14)$$

There, $\mathbf{E} = -\frac{\partial \varphi}{\partial \mathbf{x}}$ denotes the spatial electric field and ϵ the material-dependent dielectric permittivity. The corresponding material electric field is computed by the pull-back operation $\mathbf{E}_0 = \mathbf{F}^T \mathbf{E}$ with $\mathbf{E}_0 = -\frac{\partial \varphi}{\partial \mathbf{X}}$. Hence, the polarisation of the dielectric elastomer is also governed by the mechanical deformation. We further adopt the assumption from [Henann et al., 2013] and neglect the effects of free space surrounding the dielectric for simplistic reasons. Hence, the permittivity of free space ϵ_0 is set to zero. Regarding the mechanics, $\boldsymbol{\sigma}$ is decomposed into an active part $\boldsymbol{\sigma}^{\text{act}}$ and passive part $\boldsymbol{\sigma}^{\text{pas}}$. The electrical polarisation generates $\boldsymbol{\sigma}^{\text{act}}$ based on [Zhao et al., 2007], while $\boldsymbol{\sigma}^{\text{pas}}$ is purely mechanical. Additionally, we separate $\boldsymbol{\sigma}^{\text{pas}}$ into a volumetric part $\boldsymbol{\sigma}^{\text{vol}}$ and isochoric part $\boldsymbol{\sigma}^{\text{iso}}$ with $\boldsymbol{\sigma}^{\text{pas}} = \boldsymbol{\sigma}^{\text{vol}} + \boldsymbol{\sigma}^{\text{iso}}$. For the dielectric elastomer, we define $\boldsymbol{\sigma}$ as

$$\boldsymbol{\sigma} = \underbrace{\epsilon [\mathbf{E} \otimes \mathbf{E} - \frac{1}{2} (\mathbf{E} \mathbf{E}) \mathbf{I}]}_{\boldsymbol{\sigma}^{\text{act}}} + \underbrace{\kappa (J - 1) \mathbf{I}}_{\boldsymbol{\sigma}^{\text{vol}}} + \underbrace{\frac{\mu}{J} [\bar{\mathbf{b}} - \frac{1}{3} \text{tr}(\bar{\mathbf{b}}) \mathbf{I}]}_{\boldsymbol{\sigma}^{\text{iso}}} \quad (15)$$

The definition for σ^{act} is adopted from [Zhao et al., 2007] and the definition of σ^{pas} is adopted from [Bonet and Wood, 1997]. The parameters μ and λ denote the first and second Lamé's parameter and are material-dependent. The passive isotropic behaviour is described by the Neo-Hookean model for the nearly incompressible case.

3.2 Constitutive equations for the myocardium

As mentioned in Section 2.2, the term I^φ from (9) is computed based on the the Aliev-Panfilov model from [Aliev and Panfilov, 1996]. Unlike in [Göktepe and Kuhl, 2010], the term I^φ is not influenced by the mechanical deformation in our work. For further information regarding the explicit computation of I^φ , the reader is referred to [Aliev and Panfilov, 1996, Göktepe and Kuhl, 2009]. The flux vector \mathbf{q} is defined in [Göktepe and Kuhl, 2009] as

$$\mathbf{q} = d \frac{\partial \varphi}{\partial \mathbf{x}} = -d \mathbf{E} \quad (16)$$

where d is the scalar conductivity. For this work, we assume isotropy for the spatial propagation of φ . Hence, a scalar representation of the conductivity is sufficient. This assumption is made to reduce the complexity of the numerical implementation. Similar to the dielectric elastomer, we decompose σ inside the myocardial tissue into σ^{act} and σ^{pas} with an additional subdivision in σ^{vol} and σ^{iso} with $\sigma^{\text{pas}} = \sigma^{\text{vol}} + \sigma^{\text{iso}}$

$$\sigma = \underbrace{\frac{1}{J} T(\varphi) \mathbf{f} \otimes \mathbf{f}}_{\sigma^{\text{act}}} + \underbrace{\kappa(J-1) \mathbf{I}}_{\sigma^{\text{vol}}} + \underbrace{\bar{\sigma} : \mathbb{P}}_{\sigma^{\text{iso}}} \quad (17)$$

with the active fibre tension $T(\varphi)$, the spatial fibre direction $\mathbf{f} = \mathbf{F} \mathbf{f}_0$ and the modified Cauchy stress $\bar{\sigma}$. The material directions \mathbf{f}_0 and \mathbf{s}_0 define the fibre orientation of the myocardial muscle cell as illustrated in Figure 2. To

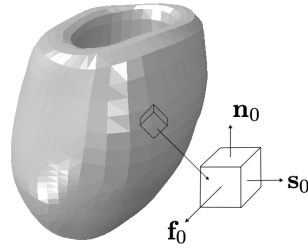


Figure 2: Anisotropic model of the myocardium. The orientation of a single myocardial cell (symbolised by a cube) is defined by an orthonormal $\mathbf{f}_0 - \mathbf{s}_0 - \mathbf{n}_0$ -basis. There, \mathbf{f}_0 denotes the fibre direction, \mathbf{s}_0 the sheet direction and \mathbf{n}_0 the normal direction in material configuration.

compute σ^{act} , $T(\varphi)$ is evaluated based on the given ordinary differential

equation in [Nash and Panfilov, 2004]

$$\dot{T} = a(\varphi)[k_T(\varphi - \varphi_r) - T] \quad (18)$$

with the control parameter k_T , the resting potential φ_r and the switch function $a(\varphi)$. The parameter k_T controls the amplitude of σ^{act} . The switch function is a smoothed form of the Heaviside step function. It is explicitly defined by

$$a(\varphi) = a_0 + (a_\infty - a_0)\exp[-\exp(-\xi(\varphi - \bar{\varphi}))] \quad (19)$$

where $\bar{\varphi}$ is the phase shift and a_0 and a_∞ are limiting parameters. In contrast to [Göktepe and Kuhl, 2010], the following inequality $a_0 > a_\infty$ must hold. This relation is proposed in [Eriksson et al., 2013] in order to achieve a temporal delay between the peak of σ^{act} and the amplitude of φ . The function approaches a_∞ for $\varphi < \bar{\varphi}$ and a_0 for $\varphi > \bar{\varphi}$. The parameter ξ controls the transition rate. A backward Euler scheme is used to compute $T(\varphi)$ iteratively.

In (17), σ^{vol} is defined by the material-dependent bulk modulus κ and σ^{iso} is computed based on the Holzapfel-Ogden model. This model was introduced in [Holzapfel et al., 2000, Holzapfel and Ogden, 2009] and expanded in [Göktepe et al., 2011] to account for nearly incompressible material. To formulate $\bar{\sigma}$, we first state the Holzapfel-Ogden strain energy function Ψ given in [Göktepe et al., 2011]

$$\Psi = \Psi^{\text{iso}} + \Psi^f + \Psi^s + \Psi^{fs} \text{ with}$$

$$\Psi^{\text{iso}} = \frac{a}{2b} \exp[b(\bar{I}_{\text{iso}} - 3)], \quad (20a)$$

$$\Psi^f = \frac{a_f}{2b_f} [\exp[b_f(\bar{I}_f - 1)^2] - 1], \quad (20b)$$

$$\Psi^s = \frac{a_s}{2b_s} [\exp[b_s(\bar{I}_s - 1)^2] - 1] \text{ and} \quad (20c)$$

$$\Psi^{fs} = \frac{a_{fs}}{2b_{fs}} [\exp[b_{fs}(\bar{I}_{fs})^2] - 1]. \quad (20d)$$

The energy is formulated in terms of the isochoric invariants \bar{I}_{iso} , \bar{I}_f , \bar{I}_s and \bar{I}_{fs} and independent material parameters a , b , a_f , b_f , a_s , b_s , a_{fs} and b_{fs} . The invariants are defined by

$$\bar{I}_{\text{iso}} = \text{tr}(\bar{\mathbf{b}}), \quad \bar{I}_f = \text{tr}(\bar{\mathbf{f}} \otimes \bar{\mathbf{f}}), \quad (21a)$$

$$\bar{I}_s = \text{tr}(\bar{\mathbf{s}} \otimes \bar{\mathbf{s}}) \text{ and } \bar{I}_{fs} = \text{tr}[(\bar{\mathbf{f}} \otimes \bar{\mathbf{s}})^{\text{sym}}] \quad (21b)$$

with the spatial isochoric directions $\bar{\mathbf{f}} = \bar{\mathbf{F}}\mathbf{f}_0$ and $\bar{\mathbf{s}} = \bar{\mathbf{F}}\mathbf{s}_0$ and the isochoric left Cauchy-Green tensor $\bar{\mathbf{b}}$ from (6). According to [Göktepe et al., 2011],

the explicit expression of $\bar{\sigma}$ is

$$\begin{aligned}\bar{\sigma} = & \frac{1}{J} \left[2 \frac{\partial \Psi^{\text{iso}}}{\partial \bar{I}_{\text{iso}}} \bar{\mathbf{b}} + 2 \frac{\partial \Psi^{\text{f}}}{\partial \bar{I}_f} \bar{\mathbf{f}} \otimes \bar{\mathbf{f}} + 2 \frac{\partial \Psi^{\text{s}}}{\partial \bar{I}_s} \bar{\mathbf{s}} \otimes \bar{\mathbf{s}} \right. \\ & \left. + \frac{\partial \Psi^{\text{fs}}}{\partial \bar{I}_{fs}} (\bar{\mathbf{f}} \otimes \bar{\mathbf{f}} + \bar{\mathbf{s}} \otimes \bar{\mathbf{s}}) \right].\end{aligned}\quad (22)$$

σ^{iso} is then computed by a double contraction between $\bar{\sigma}$ and the isochoric fourth-order projection tensor $\mathbb{P} = \mathbb{I}^{\text{sym}} - \frac{1}{3} \mathbf{I} \otimes \mathbf{I}$ in which \mathbb{I}^{sym} is the symmetric fourth-order identity tensor defined by $\mathbb{I}_{ijkl}^{\text{sym}} = \frac{1}{2} (\delta_{ik} \delta_{jl} + \delta_{il} \delta_{jk})$.

4 Numerical solution procedure using S-FEM

In this section, we summarize the numerical approximations of the governing equations and solution variables. First, some fundamentals of the FEM theory are introduced which serve as basics for S-FEM. Then, the approximation scheme using S-FEM is presented. To implement the numerical solution scheme, the discretisation of the spatial weak formulations is described. We mainly adopt the descriptions from [Wriggers, 2008] regarding the non-linear FEM and the descriptions from [Liu and Nguyen, 2010] regarding the S-FEM formulation.

4.1 Finite element method

In standard FEM, the original geometry \mathcal{B} is subdivided into so-called finite elements \mathcal{B}^e . The elements are connected to each other through nodes and form an approximation geometry \mathcal{B}^h , such that $\mathcal{B} \approx \mathcal{B}^h = \bigcup_{e=1}^{N_{el}} \mathcal{B}^e$. There, N_{el} is the total number of \mathcal{B}^e . The element-wise solution variables \mathbf{u}^e , φ^e are approximated on each \mathcal{B}^e as

$$\mathbf{u}^e = \sum_{a=1}^{n_n} \mathbf{u}^a N^a \quad \text{and} \quad (23)$$

$$\varphi^e = \sum_{a=1}^{n_n} \varphi^a N^a \quad (24)$$

where n_n is the number of element nodes and N^a is the nodal shape function. The index a denotes the local node number. Each quantity is evaluated at a and weighted by the corresponding N^a . Following the Galerkin method, the element-wise test functions \mathbf{v}_1^e , v_2^e can also be approximated by the same shape functions as

$$\mathbf{v}_1^e = \sum_{a=1}^{n_n} \mathbf{v}_1^a N^a \quad \text{and} \quad (25)$$

$$v_2^e = \sum_{a=1}^{n_n} v_2^a N^a. \quad (26)$$

For the discretisation of the weak forms from Section 2.2, the test function gradients also need to be computed element-wise. Only the shape functions are affected by the gradient operator. Therefore, the test function gradients result in

$$\frac{\partial \mathbf{v}_1^e}{\partial \mathbf{x}} = \sum_{a=1}^{n_n} \mathbf{v}_1^a \otimes \frac{\partial N^a}{\partial \mathbf{x}} \text{ and} \quad (27)$$

$$\frac{\partial v_2^e}{\partial \mathbf{x}} = \sum_{a=1}^{n_n} v_2^a \frac{\partial N^a}{\partial \mathbf{x}}. \quad (28)$$

Additionally, we can approximate the element-wise deformation gradient \mathbf{F}^e and electric field \mathbf{E}^e as

$$\mathbf{F}^e = \sum_{a=1}^{n_n} \mathbf{u}^a \otimes \frac{\partial N^a}{\partial \mathbf{X}} + \mathbf{I} \text{ and} \quad (29)$$

$$\mathbf{E}^e = - \sum_{a=1}^{n_n} \varphi^a (\mathbf{F}^e)^{-T} \frac{\partial N^a}{\partial \mathbf{X}}. \quad (30)$$

4.2 Smoothed finite element method

The basic concept behind S-FEM is to apply a smoothing operation on the gradients over defined SDs, according to [Liu et al., 2007]. The spatial body \mathcal{B} is subdivided into non-overlapping cells such that $\mathcal{B} \approx \bigcup_{k=1}^{N_s} \mathcal{B}^k$. There, \mathcal{B}^k is a SD and N_s is the total number of SDs. The resulting SD mesh is overlaid on an initial FEM mesh. This work focuses on two main smoothing methods in 3D, FS-FEM presented in [Nguyen-Thoi et al., 2009] and NS-FEM presented in [Nguyen-Thoi et al., 2010]. In FS-FEM, the smoothing domain is created around the connecting faces of neighbouring elements. First, the connecting face between two elements is identified. Then, the nodes of each face are connected with the respective element centroids to form the face-based SDs. For elements on the boundary, the nodes on the boundary face are connected to the centroid of the boundary element. The total number of SDs in FS-FEM is equal to the number of faces in the FEM mesh. In NS-FEM, each SD is created around the connecting node of adjacent elements. For each node, the connecting elements are identified. Then, the mid-points of the edges connected to the node, the connected element centroids and the centroids of the connected faces together with the node itself form the node-based SD. The volume of the node-based SD depends on the number of adjacent elements. The total number of node-based SDs is equal to the number of nodes in the FEM mesh. In this work, the SDs are constructed based on four node tetrahedral elements. In Figure 3, the resulting SDs are depicted for FS-FEM and NS-FEM. In

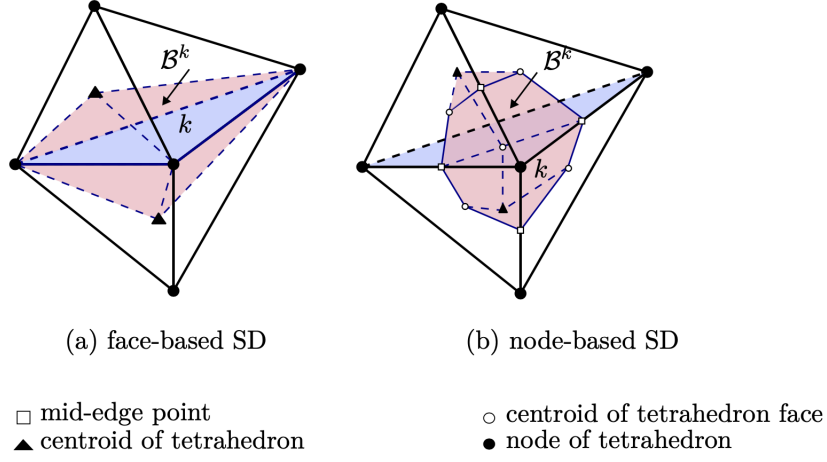


Figure 3: SDs on an initial 3D TET mesh where \mathcal{B}^k for FS-FEM is constructed around a connecting face k in (a) and for NS-FEM, \mathcal{B}^k is constructed around a connecting node k in (b) (adopted from [Martonová et al., 2023]).

[Liu et al., 2007], the following smoothing function $\Phi(\mathbf{X})$ is introduced

$$\Phi(\mathbf{X}) = \begin{cases} \frac{1}{V^k} & \text{if } \mathbf{X} \in \mathcal{B}^k \\ 0 & \text{else} \end{cases} \quad (31)$$

where V^k is the volume of the smoothing domain with $V^k = \int_{\mathcal{B}^k} dV$. Additionally, $\Phi(\mathbf{X})$ also satisfies the positivity and unity conditions

$$\Phi(\mathbf{X}) \geq 0 \text{ and } \int_{\mathcal{B}^k} \Phi(\mathbf{X}) dV = 1. \quad (32)$$

The original idea behind S-FEM is to apply $\Phi(\mathbf{X})$ to the element-wise strains connected to the respective SD leading to a smoothed deformation gradient. Using (31), the smoothed deformation gradient \mathbf{F}^k can be derived from

$$\mathbf{F}^k = \int_{\mathcal{B}^k} \frac{\partial \mathbf{u}}{\partial \mathbf{X}} \Phi(\mathbf{X}) dV + \mathbf{I} = \frac{1}{V^k} \int_{\mathcal{B}^k} \frac{\partial \mathbf{u}}{\partial \mathbf{X}} dV + \mathbf{I}. \quad (33)$$

The SDs around the faces or nodes consist of contributions from the adjacent elements. Therefore, (33) can be rewritten into

$$\mathbf{F}^k = \frac{1}{4V^k} \sum_{e=1}^{n_k} \frac{\partial \mathbf{u}}{\partial \mathbf{X}} V^e + \mathbf{I} \quad (34)$$

where n_k is the number of adjacent tetrahedrons \mathcal{B}^e around node k or face k and V^e is the volume of each \mathcal{B}^e . With further transformations and based

on [Martonová et al., 2023], (34) results in

$$\mathbf{F}^k = \frac{1}{4V^k} \sum_{e=1}^{n_k} \underbrace{\sum_{a=1}^{n_n} (\mathbf{u}^a \otimes \frac{\partial N^a}{\partial \mathbf{X}} + \mathbf{I}) V^e}_{\mathbf{F}^e} \quad (35)$$

where $n_n=4$ because of the use of tetrahedral elements. Due to the electromechanical coupling, the gradient smoothing operation also affects the electric field \mathbf{E} which results in a smoothed spatial electric field \mathbf{E}^k . Adopting the same steps used for the derivation of (35), the explicit approximation of \mathbf{E}^k results in

$$\mathbf{E}^k = -\frac{1}{4V^k} \sum_{e=1}^{n_k} \underbrace{\sum_{a=1}^{n_n} \varphi^a(\mathbf{F}^e)^{-T} \frac{\partial N^a}{\partial \mathbf{X}} V^e}_{-\mathbf{E}^e}. \quad (36)$$

Additionally to the gradient smoothing, the solution variables are also affected by the smoothing operation. The smoothed solutions \mathbf{u}^k , φ^k correspond to the solution on the SD. Applying $\Phi(\mathbf{X})$ on \mathbf{u} and φ results in

$$\mathbf{u}^k = \frac{1}{4V^k} \sum_{e=1}^{n_k} \underbrace{\sum_{a=1}^4 \mathbf{u}^a N^a V^e}_{\mathbf{u}^e} \text{ and} \quad (37)$$

$$\varphi^k = \frac{1}{4V^k} \sum_{e=1}^{n_k} \underbrace{\sum_{a=1}^4 \varphi^a N^a V^e}_{\varphi^e}. \quad (38)$$

To complete the approximations, we also state the smoothed test functions \mathbf{v}_1^k , v_2^k as

$$\mathbf{v}_1^k = \frac{1}{4V^k} \sum_{e=1}^{n_k} \underbrace{\sum_{a=1}^{n_n} \mathbf{v}_1^a N^a V^e}_{\mathbf{v}_1^e} \text{ and} \quad (39)$$

$$v_2^k = \frac{1}{4V^k} \sum_{e=1}^{n_k} \underbrace{\sum_{a=1}^{n_n} v_2^a N^a V^e}_{v_2^e}. \quad (40)$$

The smoothed test function gradients then result in

$$\frac{\partial \mathbf{v}_1^k}{\partial \mathbf{x}} = \frac{1}{4V^k} \sum_{e=1}^{n_k} \underbrace{\sum_{a=1}^{n_n} \mathbf{v}_1^a \otimes \frac{\partial N^a}{\partial \mathbf{x}}}_{\partial \mathbf{v}_1^e / \partial \mathbf{x}} V^e \text{ and} \quad (41)$$

$$\frac{\partial v_2^k}{\partial \mathbf{x}} = \frac{1}{4V^k} \sum_{e=1}^{n_k} \underbrace{\sum_{a=1}^{n_n} v_2^a \frac{\partial N^a}{\partial \mathbf{x}}}_{\partial v_2^e / \partial \mathbf{x}} V^e. \quad (42)$$

We observe, that the smoothed quantities are just the averaged values of the corresponding element-wise quantities over all elements that are connected to the SD.

4.3 Spatial discretisation and implementation

Inserting the numerical approximations from above into (11)-(13), results in the discretised weak forms which are given by local residuals for each element or SD. In S-FEM, the solution-dependent variables are evaluated inside the SD rather than inside the element. Besides the different integration domains, the discretisation procedure for S-FEM and standard FEM remains similar. In the following, we only state the local S-FEM residuals. First, the mechanical problem defined by the weak form in (11) is discretised. We adopt the assumptions from [Henann et al., 2013] and neglect the surface traction force for this work. Therefore, the local residual \mathbf{R}_u^a results in

$$\mathbf{R}_u^a = - \int_{\mathcal{B}^k} \nabla N^a \boldsymbol{\sigma} dv = \mathbf{0}. \quad (43)$$

Depending on the chosen material model, the smoothed Cauchy stress $\boldsymbol{\sigma} = \boldsymbol{\sigma}(\mathbf{F}^k, \mathbf{E}^k, \varphi^k)$ is either derived from (15) or (17). For the sake of compactness, we denote the spatial shape function gradient as $\nabla N^a = \frac{\partial N^a}{\partial \mathbf{x}}$ from now on.

The local residual for the dielectric elastomer problem $R_{\varphi, \text{die}}^a$ is derived from (12). We again adopt the assumption from [Henann et al., 2013] and neglect the surface charge. Therefore, $R_{\varphi, \text{die}}^a$ results in

$$R_{\varphi, \text{die}}^a = \int_{\mathcal{B}^k} \nabla N^a \mathbf{D} dv = 0. \quad (44)$$

The smoothed electric displacement $\mathbf{D} = \mathbf{D}(\mathbf{F}^k, \mathbf{E}^k)$ is computed using (14). For the myocardial tissue, the weak form from (13) is discretised into the local residual $R_{\varphi, \text{myo}}^a$. Based on the FEM discretisation in [Göktepe and Kuhl, 2010] and neglecting the surface flux, $R_{\varphi, \text{myo}}^a$ results in

$$R_{\varphi, \text{myo}}^a = \int_{\mathcal{B}^k} [N^a \frac{\varphi^k - \varphi_n^k}{\Delta t} + \nabla N^a \mathbf{q} dv - N^a I^\varphi] dv = 0. \quad (45)$$

In (45), the time derivative of φ is approximated by the finite difference $\frac{\varphi^e - \varphi_n^e}{\Delta t}$ where n denotes the previous time and Δt the time increment. The smoothed flux $\mathbf{q} = \mathbf{q}(\mathbf{F}^k, \mathbf{E}^k)$ is computed using (16) and the smoothed source term $I^\varphi = I^\varphi(\varphi^k)$ is computed using the Aliev-Panfilov model employed in [Göktepe and Kuhl, 2009]. For each element, a local residual $\mathbf{R}^a = (\mathbf{R}_u^a, R_\varphi^a)^T$ is constructed consisting of the mechanical part \mathbf{R}_u^a and the electrical part R_φ^a . Depending on the material, either (44) or (45) are used for R_φ^a . To solve the resulting non-linear system of equations in \mathbf{R}^a , the Newton-Raphson method is employed. For the general theory behind this numerical scheme, the reader is referred to [Wriggers, 2008]. A more detailed description of the resulting tangent stiffness matrices is presented in Appendix A.1 and A.2 at the end of this paper.

In this work, we implemented the numerical framework for standard FEM, FS-FEM, NS-FEM and FSNS-FEM into Abaqus through customized user element subroutines (UELs). A Matlab script was used to create a user-defined mesh based on an initial TET mesh. The individual user elements of this mesh represent the face-based or node-based SDs. For FSNS-FEM, a node-based SD mesh was overlaid on a face-based SD mesh. The UEL computes and returns the right-hand-side and tangent stiffness matrix of the linearised local residual \mathbf{R}^a for each user element. For further information regarding the creation and structure of an UEL, the reader is referred to the Abaqus documentation [Dassault Systems, 2016]. After the UEL computes and returns the local quantities, the solver then assembles them into a global system of equations and computes the node-wise solutions. The workflow is schematically displayed in Figure 4. We adopted the UEL code structure

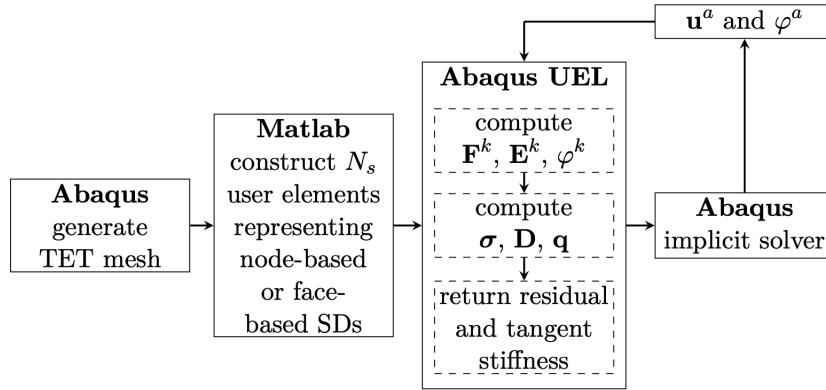


Figure 4: Generalised workflow of the major steps to implement S-FEM into Abaqus for electromechanically coupled problems.

from [Wang et al., 2016] and implemented the computation of the smoothed kinematic and constitutive quantities based on [Martonová et al., 2023] for the dielectric elastomer and the myocardial tissue. In Table 1, we summarise

the numerical methods used for the dielectric elastomer problem. For each numerical method, the table identifies on which element or SD, σ^{act} , σ^{vol} , σ^{iso} and \mathbf{D} are computed to construct the local residual. The corresponding tangent stiffness matrix is also computed on the respective element or SD. In

method/discretisation	TET	face-based SD	node-based SD
FEM	σ, \mathbf{D}		
FS-FEM		σ, \mathbf{D}	
NS-FEM			σ, \mathbf{D}
FSNS-FEM		$\sigma^{\text{act}}, \sigma^{\text{iso}}, \mathbf{D}$	σ^{vol}

Table 1: Numerical methods used for the dielectric elastomer problem. For each S-FEM, σ and \mathbf{D} are either being evaluated inside the face-based SDs or node-based SDs or both. For standard FEM, σ and \mathbf{D} are either being evaluated inside the TET elements.

the same manner, we summarise the numerical methods for the myocardial tissue problem in Table 2. In contrast to the proposed discretisation in (45), $\dot{\varphi}$ and I^φ are not computed inside the SD for the S-FEMs but on the TET mesh. This work only observes the smoothing effects on the electromechanically coupled variables, namely $\sigma(\mathbf{F}^k, \varphi^k)$, $\mathbf{D}(\mathbf{F}^k, \mathbf{E}^k)$ and $\mathbf{q}(\mathbf{F}^k, \mathbf{E}^k)$. For that reason and to ensure comparability between the different methods, the temporal evolution and source are evaluated on the same TET mesh, see Table 2.

method/discretisation	TET	face-based SD	node-based SD
FEM	$\sigma, \dot{\varphi}, \mathbf{q}, I^\varphi$		
FS-FEM	$\dot{\varphi}, I^\varphi$	σ, \mathbf{q}	
NS-FEM	$\dot{\varphi}, I^\varphi$		σ, \mathbf{q}
FSNS-FEM	$\dot{\varphi}, I^\varphi$	$\sigma^{\text{act}}, \sigma^{\text{iso}}, \mathbf{q}$	σ^{vol}

Table 2: Numerical methods used for the myocardial contraction. For each S-FEM, σ and \mathbf{q} are either being evaluated inside the face-based SDs or node-based SDs or both. For standard FEM, σ and \mathbf{q} are either being evaluated inside the TET elements. For each method, $\dot{\varphi}$ and I^φ are evaluated inside the TET elements.

5 Numerical examples

In this section, the implementations of the numerical methods are tested and evaluated with respect to their accuracy and simulation time. A cube model representing a simplified DEA and a section of the myocardium serves as benchmark.

5.1 Coupled DEA cube

For the dielectric elastomer problem, we tested the implementations of the numerical methods on a simple electromechanically coupled cube with passive nearly incompressible Neo-Hookean material. The edge length was set to $l = 10$ mm. We defined 256 nodes within the geometry which results into a discretisation of 1050 TET elements for FEM (TET-FEM), 2250 face-based SDs for FS-FEM and 256 node-based SDs for NS-FEM. For FSNS-FEM, 256 node-based SDs are over-layered on top of 2250 face-based SDs. The material-dependent parameters necessary to describe the mechanical and electrical behaviour are summarised in Table 3. The cube was fixed in three

μ [kPa]	λ [kPa]	ϵ [Fmm ⁻²]
2000	666.67	1

Table 3: Material parameters necessary to describe the passive and active behaviour of the DEA cube.

directions preventing a rigid body motion and actuated by an external potential. The external potential was partially applied on the cube's front face and varied over time. We defined it as an electrical boundary condition $\bar{\varphi}(t)$. The potential on the opposite face was fixed at $\bar{\varphi}_0 = 0$ mV. The simulation setup is depicted in Figure 5. Here, \mathcal{S} defines the excitation surface

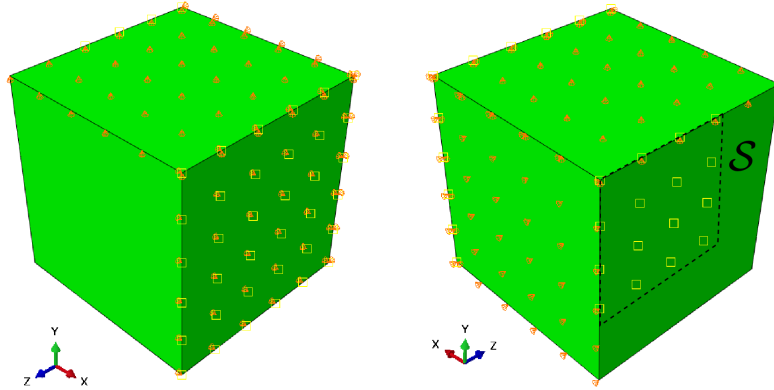


Figure 5: Location of the mechanical (orange cones) and electrical (yellow squares) boundary conditions for the DEA cube simulation. The displacement of the nodes on the excited surface \mathcal{S} are later evaluated.

on which $\bar{\varphi}(t)$ is applied. The contraction simulation was carried out in two steps. First, $\bar{\varphi}(t)$ is linearly increased from 0 mV to 100 mV over a time span of 50 ms. This lead to a compression of the cube. We denote the first step as the loading step. Second, $\bar{\varphi}(t)$ was linearly decreased back to 0 mV over a time span of 50 ms. The cube then returned back to its undeformed

state. We denote the second step as unloading step. Additionally, a reference simulation on a hexahedral mesh (HEX) with 125 fully integrated elements was conducted to evaluate the accuracy of our implementations. We will denote the reference simulation as HEX-FEM. In Figure 6, snapshots taken in Abaqus at $t = 50$ ms for each numerical method are depicted showing the nodal displacement magnitudes $\|\mathbf{u}\|$ in mm. The compression of the cube's front face is clearly visible with indentations around \mathcal{S} . To

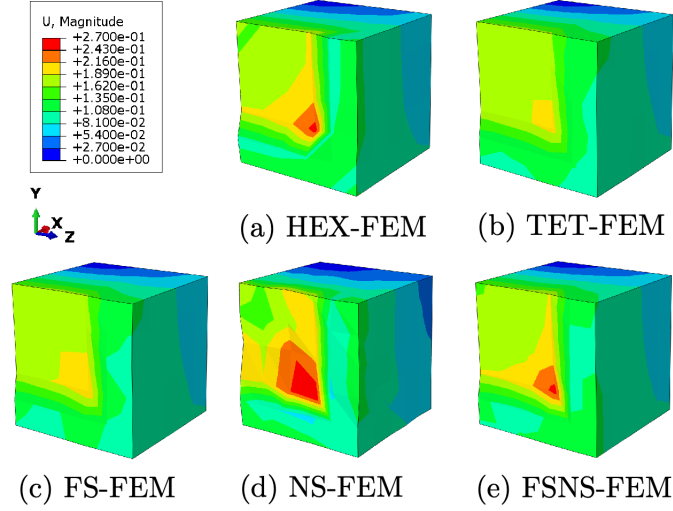


Figure 6: Snapshot taken at $t = 50$ ms in Abaqus of the displacement magnitude $\|\mathbf{u}\|$ in mm for each numerical method.

further compare the different solutions over time, we used a scalar representation of the deformation at each time. Therefore, the nodal displacement solutions on \mathcal{S} were averaged at specific times with a constant increment of $\Delta t = 5$ ms. The resulting deformation curves are depicted in Figure 7. For each method, the curve starts at 0 mm and monotonically increases until it reaches its amplitude at $t = 50$ ms. Then, the curve decreases monotonically until the initial. We observe that the simulations using TET-FEM and FS-FEM yield deformations that are below the reference solution. This indicates an overestimated stiffness caused by volumetric locking for both methods. This phenomenon appears in linear TET meshes combined with nearly incompressible material behaviour according to [Liu, 2019]. The simulation using NS-FEM yields a deformation curve which is above the reference solution. This indicates an overestimated softness which corresponds to the limitations of NS-FEM stated in [Wang et al., 2015]. The simulation using FSNS-FEM returns results which are nearly identical to the reference solution indicating a high accuracy. For each S-FEM and TET-FEM we

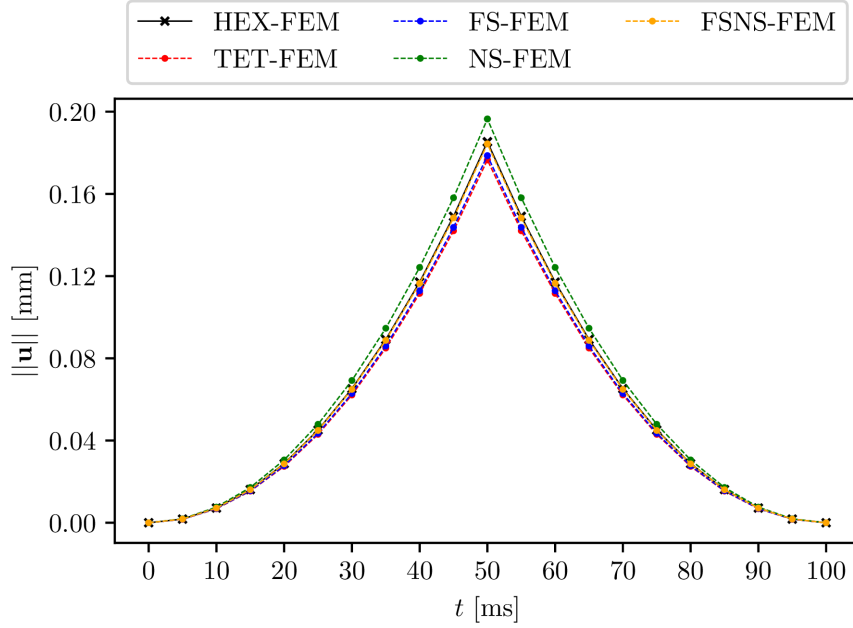


Figure 7: Averaged displacement magnitude $\|u\|$ on excited surface \mathcal{S} during the loading step $t \in [0, 50]$ ms and unloading step $t \in [50, 100]$ ms for each method.

compute the relative error averaged over all n_t time steps with

$$\bar{e}_r = \frac{1}{n_t} \sum_{i=1}^{n_t} \left| 1 - \frac{\|u\|_i}{\|u\|_i^{\text{ref}}} \right| \quad (46)$$

where $\|u\|_i$ is the averaged displacement magnitude at time step i of the respective method depicted in Figure 7 and $\|u\|_i^{\text{ref}}$ is the reference obtained by HEX-FEM. The results are listed in Table 4 together with the total central processing unit (CPU) times of each S-FEM and TET-FEM simulation. The

method	\bar{e}_r [-]	CPU time [s]
TET-FEM	0.047	299.9
FS-FEM	0.036	39.3
NS-FEM	0.061	11.0
FSNS-FEM	0.005	61.7

Table 4: Mean relative error \bar{e}_r over simulation time with respect to HEX-FEM and total CPU time for each numerical method.

NS-FEM simulation runs the shortest with a CPU time of 11 s but produces results with the highest error with $\bar{e}_r = 6.1\%$. The remaining methods return

sufficiently accurate solutions where the error is below 5 %. The simulation using TET-FEM runs the longest with a CPU time of around 300 s which is nearly five times higher than the second longest simulation using FSNS-FEM. This result highlights the inefficiency of using TET-FEM compared to FS-FEM and FSNS-FEM. The FSNS-FEM simulation has the smallest error with $\bar{\epsilon}_r = 0.5$ % with a total CPU time of 61.7 ms which is nearly five times shorter than for TET-FEM but still the second longest simulation. The FS-FEM simulation runs second shortest with a total CPU time of 39.3 s and an error of $\bar{\epsilon}_r = 3.6$ %. However, the observation in Figure 7 shows an overestimation of the stiffness over time when using FS-FEM. Therefore, we conclude that FSNS-FEM is the most suitable method to simulate the dielectric elastomer problem because it overcomes the overly-stiff behaviour of TET elements without overestimating the softness resulting in the most accurate solution with an error below 1 % which is a sufficient trade-off for the longer CPU time.

5.2 Coupled myocardial cube

For this numerical example, the used geometry represents a section of the myocardium where the front face represents the sub-epicardium and the back face represents the sub-endocardium. The same cube model with an identical discretisation as for the dielectric problem was utilized. In summary, 256 nodes were defined, resulting in a mesh consisting of 1050 TET elements for TET-FEM, 2250 face-based SDs for FS-FEM, 256 node-based SDs for NS-FEM, and a combination of face-based/node-based SDs for FSNS-FEM. To mimic the orthotropic behaviour of the myocardium based on the Holzapfel-Ogden model, given in (20), we implemented rule-based local fibre, sheet and sheet-normal directions, \mathbf{f}_0 , \mathbf{s}_0 and \mathbf{n}_0 , respectively. Globally, the fibres were aligned by $+60^\circ$ on the sub-epicardium (front face in Figure 8.a) and -60° on the sub-endocardium (back face in Figure 8.a) with respect to the global y -axis. The rotation of the fibres throughout the myocardium is fairly smooth. For the TET mesh, we assigned a local $\mathbf{f}_0^e - \mathbf{s}_0^e - \mathbf{n}_0^e$ coordinate system to each element e . For S-FEM, the coordinate system was assigned to each SD. To compute the smoothed directional vectors $\mathbf{f}_0^k - \mathbf{s}_0^k - \mathbf{n}_0^k$, we adopted the rule from [Martonová et al., 2023]. There, the local coordinate system of the face-based or node-based SD is derived by averaging the $\mathbf{f}_0^e - \mathbf{s}_0^e - \mathbf{n}_0^e$ from each element connected to either face k or node k with

$$\mathbf{f}_0^k = \frac{1}{n_k} \sum_{e=1}^{n_k} \mathbf{f}_0^e, \quad \mathbf{s}_0^k = \frac{1}{n_k} \sum_{e=1}^{n_k} \mathbf{s}_0^e \quad \text{and} \quad \mathbf{n}_0^k = \frac{1}{n_k} \sum_{e=1}^{n_k} \mathbf{n}_0^e. \quad (47)$$

In Figure 8, the material \mathbf{f}_0 -, \mathbf{s}_0 and \mathbf{n}_0 - axes are depicted for each TET element. There, the front face at $(x, y, z = 0)$ mm represents the sub-epicardium and the back face at $(x, y, z = 10)$ mm represent the sub-endocardium. To compute the passive stress in (17), we adopted the pa-

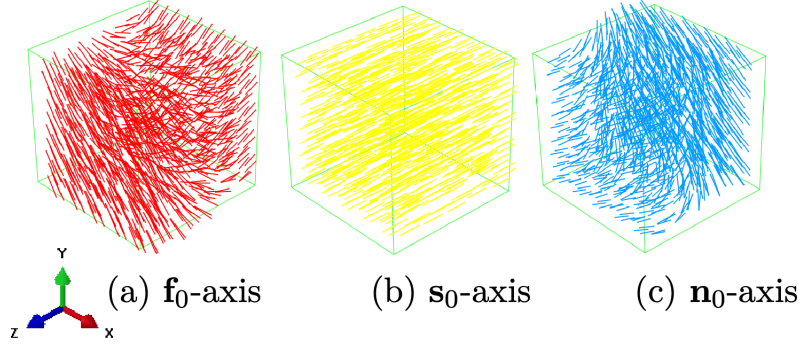


Figure 8: Material \mathbf{f}_0 -, \mathbf{s}_0 - and \mathbf{n}_0 - directions for each TET element. The fibre direction \mathbf{f}_0 rotates smoothly from $+60^\circ$ on the front face to -60° on the back face with respect to the global y -axis. The sheet direction \mathbf{s}_0 is aligned to the global z -axis for each element. The normal direction \mathbf{n}_0 results from the normalized cross-product between \mathbf{f}_0 and \mathbf{s}_0 .

rameters given in [Martonova et al., 2021]. There, the strain-energy from (20) was fitted to experimental data obtained from an uniaxial extension test and simple shear test conducted simultaneously. For the calculation

κ [kPa]	a [kPa]	b [-]	a_f [kPa]	b_f [-]	a_s [kPa]	b_s [-]	a_{fs} [kPa]	b_{fs} [-]
1000	1.665	1.237	7.822	0.008	0	0	1.342	9.178

Table 5: Material parameters necessary to describe the passive behaviour of the myocardial cube based on the Holzapfel-Ogden model.

of the active stress in (17), we used the parameters summarised in Table 6. There, the values were chosen to achieve stable simulations for each method. To account for the electrical flux \mathbf{q} , the scalar conductivity from (14) was set

k_T [kPamV $^{-1}$]	a_0 [mV $^{-1}$]	a_∞ [mV $^{-1}$]	ξ [mV $^{-1}$]	φ_r [mV]	$\bar{\varphi}$ [mV]
0.005	1	0.1	0.1	-80	-80

Table 6: Material parameters necessary to describe the active behaviour of the myocardial cube.

to $d = 0.01 \text{ mm}^2 \text{ms}^{-1}$. For simplistic reasons, we assumed that the resulting orthotropic material behaviour does not affect the spatial propagation of the electric potential φ . Therefore, \mathbf{q} is independent of the fibre-orientations. The coupled contraction simulation was run in three steps. In the initial step, each node inside the cube were polarised at -80 mV for 1 ms . In the next step, the nodal potentials in a specified region were increased to -60 mV for 1 ms . The used activation node-set was constructed to enable a stable simulation for each method. The chosen activation region together with

the mechanical boundary conditions for the simulation are shown in Figure 9. This activation step triggers the generation of electric potential and

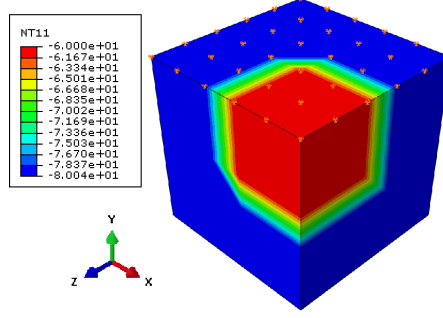


Figure 9: The nodes inside the activation region (red) are depolarised from -80 mV to -60 mV which generates an electric field inside the cube and triggers the generation of electric potential based on the Aliev-Paniflov model. The mechanical boundary conditions are visualised by the orange cones. The nodes on the top face at $(x, y = 10, z)$ mm are fixed in all spatial directions.

an electric Field. As shown in Table 2, the electric potential is generated on the TET mesh for each method. The electric field is either generated on the TET mesh or the SD mesh. In the last step, all electric boundary conditions were omitted. The source term I^φ governs the generation and temporal evolution of the electric potential and the electric field \mathbf{E} governs the spatial propagation of the electric potential which results in the deformation of the cube. The contraction step was defined for 180 ms. For all steps, the nodes at the cube's top were fixed in each direction to prevent translation. Similar to the dielectric problem, a reference simulation on a hexahedral (HEX) mesh with 125 fully integrated elements was conducted to evaluate the accuracy of the numerical methods. In Figure 10, snapshots taken in Abaqus at $t = 75$ ms for each numerical method are depicted showing the nodal displacement magnitude $\|\mathbf{u}\|$ in mm on the cube's bottom at $(x, y = 0, z)$ mm. The observed deformation modes indicate compression and torsion of the cube for each method. The largest displacement appears in the outer corner, while the centre remains nearly static. Similar to the dielectric problem, we used a scalar representation of the deformation to compare each method. Therefore, the nodal displacement magnitudes at the cube's bottom were averaged at specific times with a constant increment of $\Delta t = 5$ ms. The resulting deformation curves for the contraction step are depicted in Figure 11. The reference solution curve and the curves obtained from NS-FEM and FSNS-FEM increase until their respective amplitudes are reached at $t = 75$ ms and then decrease back to the undeformed state. Observing the results from TET-FEM and FS-FEM, the curves first increase until $t = 40$ ms and the decrease for two time steps. This valleys in

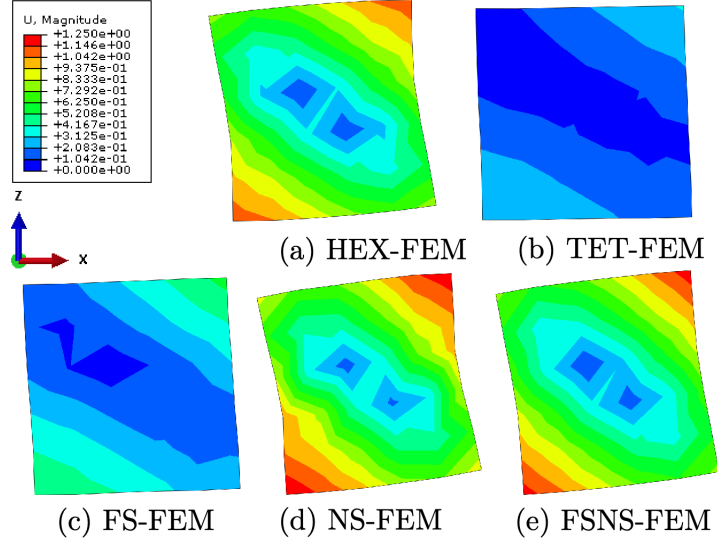


Figure 10: Snapshot taken at $t = 75$ ms of the displacement magnitude $||u||$ in mm for each numerical method. We observe the bottom face of the cube at $(x, y = 0, z)$ mm.

method	$\bar{\epsilon}_r$ [-]	CPU time [s]
TET-FEM	0.686	614.4
FS-FEM	0.533	72.9
NS-FEM	0.115	43.9
FSNS-FEM	0.028	228.0

Table 7: Mean relative error $\bar{\epsilon}_r$ over simulation time with respect to the HEX-FEM solution and total CPU time for each numerical method.

combination with the stiffer behaviour indicate the appearance of volumetric locking, similar to the dielectric problem. Using FS-FEM reduces the volumetric locking but the material behaviour is still considerably stiff. Using NS-FEM, the deformation is larger than the reference which indicates an overestimated softness, similar to the observation from the DEA problem. The results obtained from the FSNS-simulation are in best agreement with the reference solutions. For each S-FEMs and TET-FEM we again compute $\bar{\epsilon}_r$ using (46). The results are listed in Table 7 together with the total CPU time for each method. The use of TET-FEM results in the largest error with $\bar{\epsilon}_r = 68.6$ % and takes the longest with a CPU time of 614.4 s. Similar to the DEA example, this method tends to be relatively ineffective. The simulation using NS-FEM runs the fastest and produces the second smallest error with $\bar{\epsilon}_r = 11.5$ %. The use of FS-FEM results in the second-fastest simulation with a CPU time of 72.9 s. Nevertheless, an error of $\bar{\epsilon}_r = 53.3$ %

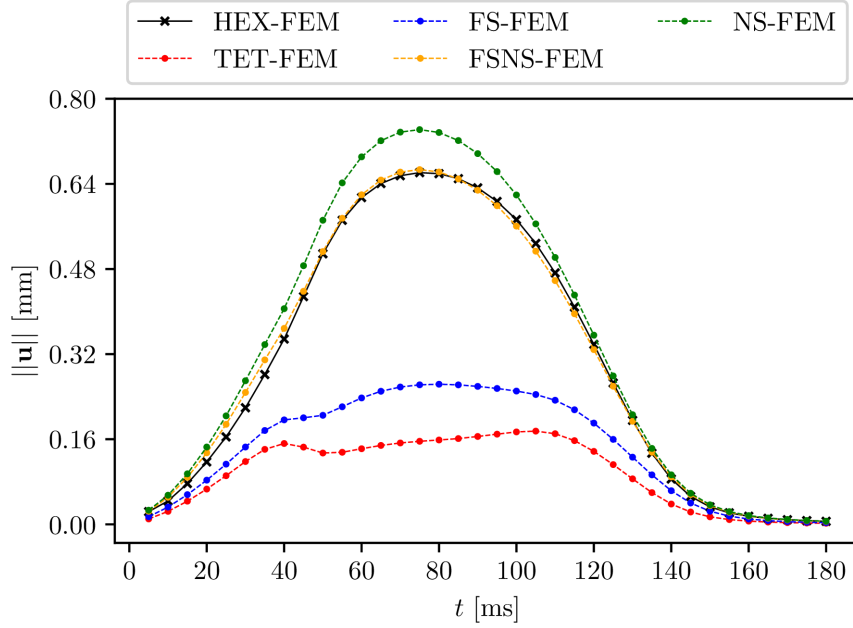


Figure 11: Averaged displacement magnitude $\|\mathbf{u}\|$ on bottom face at $(x, y = 0, z)$ mm during the contraction step $t \in [0, 180]$ ms for each method.

renders this method still ineffective. The solution obtained from the FSNS-FEM simulation shows the best approximation with an error of $\bar{e}_r = 2.8$ %. Relative to FS-FEM and NS-FEM, FSNS-FEM still requires a longer CPU time with 228 s. Nevertheless, we still conclude FSNS-FEM to be the most suitable method to simulate the myocardial tissue because it overcomes the volumetric locking with a small enough error which compensates for the longer CPU time.

6 Concluding remarks

Conclusion

In this work, we used linear FEM and various S-FEMs to numerically approximate and solve the electromechanically coupled problem for a dielectric elastomer and myocardial tissue. The commercial software Abaqus served as the simulation environment, with electromechanically coupled UELs implemented using TET-FEM, FS-FEM, NS-FEM, and FSNS-FEM. Two numerical examples were simulated: the electrically induced contraction of a DEA and a myocardial tissue sample.

For both cases, a cube served as the benchmark geometry. In the DEA example, passive material behaviour was modelled by the nearly incom-

pressible Neo-Hookean energy function, and active behaviour by the ideal dielectric elastomer energy function. Contraction was induced through a temporally varying external potential, with a HEX mesh reference solution used for comparison. TET-FEM and FS-FEM overestimated stiffness due to volumetric locking, NS-FEM overestimated softness, while FSNS-FEM delivered the closest match to the reference solution, achieving high accuracy at relatively low computational cost thanks to the use of linear shape functions.

In the myocardium example, the nearly incompressible Holzapfel–Ogden energy function was used to model passive behaviour, with orthotropy incorporated via local fibre directions. Contraction was triggered via depolarising a certain node set. The electric field differed between methods due to gradient smoothing effects, influencing the resulting contraction. Comparisons with the HEX mesh again showed high volumetric locking for TET-FEM, reduced locking for S-FEMs, persistent stiffness/softness tendencies for FS-FEM and NS-FEM, and the highest accuracy for FSNS-FEM.

While FSNS-FEM proved to be the most accurate method for both benchmark problems, the simplified cube geometries and boundary conditions limit the physiological realism of the current simulations. Future work incorporating anatomically realistic geometries, refined boundary conditions, and more advanced constitutive models could improve predictive capacity. Overall, FSNS-FEM emerged as a robust and reliable approach for simulating the electromechanical behaviour of both dielectric elastomers and myocardial tissue, consistently achieving high accuracy at relatively low computational cost. These results underscore its strong potential for more realistic and clinically relevant electromechanical simulations, paving the way for advanced tissue modelling and patient-specific computational studies.

Acknowledgements

This work is funded by the Deutsche Forschungsgemeinschaft (DFG, German Research Foundation) project no. 496647562.

Declaration of competing interests

There is no conflict of interest to declare.

Supplementary material

After publication of the final version of the manuscript, an implementation of all the user element subroutines will be available at our Github repository https://github.com/TanTran1512/SFEM_electromechanics.

A Linearisation of the local residuals

To numerically solve the non-linear coupled problem given by $\mathbf{R}^a = (\mathbf{R}_{\mathbf{u}}^a, R_{\varphi}^a)^T = \mathbf{0}$, the Newton-Raphson scheme was employed for this work. The necessary linearisation of \mathbf{R}^a results in the following tangent stiffness matrices

$$\mathbf{K}_{\mathbf{uu}}^{ab} = -\frac{\partial \mathbf{R}_{\mathbf{u}}^a}{\partial \mathbf{u}^b}, \quad \mathbf{K}_{\mathbf{u}\varphi}^{ab} = -\frac{\partial \mathbf{R}_{\mathbf{u}}^a}{\partial \varphi^b}, \quad (48a)$$

$$\mathbf{K}_{\varphi\mathbf{u}}^{ab} = -\frac{\partial R_{\varphi}^a}{\partial \mathbf{u}^b} \text{ and } \mathbf{K}_{\varphi\varphi}^{ab} = -\frac{\partial R_{\varphi}^a}{\partial \varphi^b}. \quad (48b)$$

Assembling the individual tangents leads to the local tangent stiffness matrix \mathbf{K}^{ab} . The computation of the tangents differs between the coupled problem formulations of the dielectric elastomer and the myocardium. To implement the numerical scheme for the coupled dielectric elastomer, we adopt the formulations given in [Henann et al., 2013]. For the coupled myocardial problem, we adopt the formulations given in [Göktepe and Kuhl, 2010]. In both works, the governing equations are given for FEM. The procedure is equivalent for S-FEM. In the following, we only state the tangent expressions for S-FEM.

A.1 Dielectric elastomer formulation

Linearising the mechanical residual $\mathbf{R}_{\mathbf{u}}^a$ from (43) with respect to \mathbf{u} , results into the following explicit expression of $\mathbf{K}_{\mathbf{uu}}^{ab}$

$$\mathbf{K}_{\mathbf{uu}}^{ab} = \int_{\mathcal{B}^k} \nabla N^a : \mathbb{C}_{\mathbf{uu}} : \nabla N^b dv + \int_{\mathcal{B}^k} (\nabla N^a \boldsymbol{\sigma} \nabla N^b) \mathbf{I} dv \quad (49)$$

There, the first part describes the material non-linearity governed by the fourth-order spatial elasticity tensor $\mathbb{C}_{\mathbf{uu}}$. According to [Federico, 2012], $\mathbb{C}_{\mathbf{uu}}$ is defined by the push-forward of the material elasticity tensor with

$$\mathbb{C}_{\mathbf{uu}} = \frac{1}{J} (\mathbf{F}^k \otimes \mathbf{F}^k) : 2 \frac{\partial \mathbf{S}}{\partial \mathbf{C}^k} : (\mathbf{F}^k \otimes \mathbf{F}^k)^T \quad (50)$$

where $\mathbf{S} = J(\mathbf{F}^k)^{-1} \boldsymbol{\sigma} (\mathbf{F}^k)^{-T}$ denotes the second Piola-Kirchhoff stress tensor. The second part describes the geometric non-linearity governed by the Cauchy stress $\boldsymbol{\sigma}$ from (15) consisting of the passive part and active part. Evaluating the remaining tangents, results in the following expressions

$$\mathbf{K}_{\mathbf{u}\varphi}^{ab} = \int_{\mathcal{B}^k} \nabla N^a : \mathbb{C}_{\mathbf{u}\varphi} : \nabla N^b dv, \quad (51)$$

$$\mathbf{K}_{\varphi\mathbf{u}}^{ab} = - \int_{\mathcal{B}^k} \nabla N^a : \mathbb{C}_{\varphi\mathbf{u}} : \nabla N^b dv \text{ and } \quad (52)$$

$$\mathbf{K}_{\varphi\varphi}^{ab} = - \int_{\mathcal{B}^k} \nabla N^a \mathbb{C}_{\varphi\varphi} \nabla N^b dv. \quad (53)$$

There, the sensitivities $\mathbb{C}_{\mathbf{u}\varphi}$, $\mathbb{C}_{\varphi\mathbf{u}}$ and $\mathbb{C}_{\varphi\varphi}$ are formulated in terms of partial derivatives. We adopt the definitions given in [Henann et al., 2013]

$$\mathbb{C}_{\mathbf{u}\varphi} = -\frac{\partial \boldsymbol{\sigma}}{\partial \mathbf{E}^k}, \quad \mathbb{C}_{\varphi\mathbf{u}} = \frac{\partial \mathbf{D}}{\partial \mathbf{F}^k} \mathbf{F}^k \quad \text{and} \quad \mathbb{C}_{\varphi\varphi} = -\frac{\partial \mathbf{D}}{\partial \mathbf{E}^k}. \quad (54)$$

An explicit calculation of the above expressions can be found in our code implementations.

A.2 Myocardium formulation

The linearisation of the mechanical residual for the coupled myocardial problem, results into the same form from (49). There, the spatial elasticity tensor $\mathbb{C}_{\mathbf{uu}}$ is computed from the passive Holzapfel-Ogden model. According to [Göktepe and Kuhl, 2010], we have

$$\begin{aligned} \mathbb{C}_{\mathbf{uu}} = & \kappa J(2J - 1) \mathbf{I} \otimes \mathbf{I} - 2\kappa(J^2 - 1) \mathbb{I}^{\text{sym}} \\ & + \mathbb{P} : [\bar{\mathbb{C}} + \frac{2}{3}(J\bar{\boldsymbol{\sigma}} : \mathbf{I}) \mathbb{I}^{\text{sym}}] : \mathbb{P} - \frac{2}{3}(\mathbb{P} : J\boldsymbol{\sigma} \otimes \mathbf{I} + \mathbf{I} : J\bar{\boldsymbol{\sigma}} \otimes \mathbb{P}) \end{aligned} \quad (55)$$

with the modified Cauchy stress $\bar{\boldsymbol{\sigma}}$ from (22) and a modified elasticity tensor $\bar{\mathbb{C}}$. The explicit form is also given in [Göktepe and Kuhl, 2010] by

$$\begin{aligned} \bar{\mathbb{C}} = & 4 \frac{\partial \Psi^{\text{iso}}}{\partial \bar{I}_{\text{iso}}} (\bar{\mathbf{b}}^k \otimes \bar{\mathbf{b}}^k) + 4 \frac{\partial \Psi^{\text{f}}}{\partial \bar{I}_{\text{f}}} (\bar{\mathbf{f}}^k \otimes \bar{\mathbf{f}}^k \otimes \bar{\mathbf{f}}^k \otimes \bar{\mathbf{f}}^k) \\ & + 4 \frac{\partial \Psi^{\text{s}}}{\partial \bar{I}_{\text{s}}} (\bar{\mathbf{s}}^k \otimes \bar{\mathbf{s}}^k \otimes \bar{\mathbf{s}}^k \otimes \bar{\mathbf{s}}^k) \\ & + \frac{\partial \Psi^{\text{fs}}}{\partial \bar{I}_{\text{fs}}} (\bar{\mathbf{f}}^k \otimes \bar{\mathbf{s}}^k + \bar{\mathbf{s}}^k \otimes \bar{\mathbf{f}}^k) \otimes (\bar{\mathbf{f}}^k \otimes \bar{\mathbf{s}}^k + \bar{\mathbf{s}}^k \otimes \bar{\mathbf{f}}^k) \end{aligned} \quad (56)$$

in terms of the isochoric left Cauchy-Green tensor from (6), the scalar derivatives of the isochoric invariants from (21) and the smoothed isochoric directions from (47). Evaluating the remaining tangents, results in the following expressions

$$\mathbf{K}_{\mathbf{u}\varphi}^{ab} = \int_{\mathcal{B}^k} (\nabla N^a \mathbb{C}_{\mathbf{u}\varphi}) N^b dv, \quad (57)$$

$$\mathbf{K}_{\varphi\mathbf{u}}^{ab} = - \int_{\mathcal{B}^k} \nabla N^a : \mathbb{C}_{\varphi\mathbf{u}} : \nabla N^b dv \quad \text{and} \quad (58)$$

$$\mathbf{K}_{\varphi\varphi}^{ab} = \int_{\mathcal{B}^k} [-N^a \frac{1}{\Delta t} N^b - \nabla N^a \mathbb{C}_{\varphi\varphi} \nabla N^b + N^a \frac{\partial I^\varphi}{\partial \varphi^k} N^b] dv. \quad (59)$$

The sensitivities are computed based on the following partial derivatives

$$\mathbb{C}_{\mathbf{u}\varphi} = \frac{\partial \boldsymbol{\sigma}}{\partial \varphi^k}, \quad \mathbb{C}_{\varphi\mathbf{u}} = \frac{\partial \mathbf{q}}{\partial \mathbf{F}^k} \mathbf{F}^k \quad \text{and} \quad \mathbb{C}_{\varphi\varphi} = -\frac{\partial \mathbf{q}}{\partial \mathbf{E}^k}. \quad (60)$$

To obtain $\mathbb{C}_{\mathbf{u}\varphi}$, the definition in [Göktepe and Kuhl, 2010] was used. Due to the similar formulation between \mathbf{D} and \mathbf{q} , the implementation of $\mathbb{C}_{\varphi\mathbf{u}}$ and $\mathbb{C}_{\varphi\varphi}$ was based on [Henann et al., 2013]. As mentioned previously, the source term is computed on the TET mesh instead of the SD mesh. Therefore, the tangent stiffness $\mathbf{K}_{\varphi\varphi}^{ab}$ for S-FEM implemented with the terms $\frac{1}{\Delta t} = 0$ and $\frac{\partial I^\varphi}{\partial \varphi^k} = 0$. The temporal evolution of φ is computed inside an additional user subroutine called HETVAL. This subroutine is originally used to define heat generation inside an element. In our work it is used to define the generation and evolution over time of φ inside the TET element. An explicit computation of the sensitivities and resulting tangent stiffness matrices can be found in our code implementations.

References

- [Aliev and Panfilov, 1996] Aliev, R. R. and Panfilov, A. V. (1996). A simple two-variable model of cardiac excitation. *Chaos, Solitons & Fractals*, 7(3):293–301.
- [Bonet and Wood, 1997] Bonet, J. and Wood, R. D. (1997). *Nonlinear continuum mechanics for finite element analysis*. Cambridge Univ. Press, Cambridge.
- [Cai and Zhou, 2019] Cai, B. and Zhou, L. (2019). A coupling electromechanical inhomogeneous cell-based smoothed finite element method for dynamic analysis of functionally graded piezoelectric beams. *Advances in Materials Science and Engineering*, 2019(1).
- [Dassault Systems, 2016] Dassault Systems (2016). Abaqus online documentation.
- [Eriksson et al., 2013] Eriksson, T. S. E., Prassl, A. J., Plank, G., and Holzapfel, G. A. (2013). Modeling the dispersion in electromechanically coupled myocardium. *International Journal for Numerical Methods in Biomedical Engineering*, 29(11):1267–1284.
- [Federico, 2012] Federico, S. (2012). Covariant formulation of the tensor algebra of non-linear elasticity. *International Journal of Non-Linear Mechanics*, 47(2):273–284. Nonlinear Continuum Theories.
- [Göktepe et al., 2011] Göktepe, S., Acharya, S. N. S., Wong, J., and Kuhl, E. (2011). Computational modeling of passive myocardium. *International Journal for Numerical Methods in Biomedical Engineering*, 27(1):1–12.
- [Göktepe and Kuhl, 2009] Göktepe, S. and Kuhl, E. (2009). Computational modeling of cardiac electrophysiology: A novel finite element approach. *International Journal for Numerical Methods in Engineering*, 79(2):156–178.

- [Göktepe and Kuhl, 2010] Göktepe, S. and Kuhl, E. (2010). Electromechanics of the heart: a unified approach to the strongly coupled excitation–contraction problem. *Computational Mechanics*, 45(2-3):227–243.
- [Henann et al., 2013] Henann, D. L., Chester, S. A., and Bertoldi, K. (2013). Modeling of dielectric elastomers: Design of actuators and energy harvesting devices. *Journal of the Mechanics and Physics of Solids*, 61(10):2047–2066.
- [Holzapfel et al., 2000] Holzapfel, G. A., Gasser, T. C., and Ogden, R. W. (2000). A new constitutive framework for arterial wall mechanics and a comparative study of material models. *Journal of Elasticity*, 61(1/3):1–48.
- [Holzapfel and Ogden, 2009] Holzapfel, G. A. and Ogden, R. W. (2009). Constitutive modelling of passive myocardium: a structurally based framework for material characterization. *Philosophical transactions. Series A, Mathematical, physical, and engineering sciences*, 367(1902):3445–3475.
- [Jiang et al., 2014] Jiang, C., Zhang, Z.-Q., Han, X., and Liu, G.-R. (2014). Selective smoothed finite element methods for extremely large deformation of anisotropic incompressible bio-tissues. *International Journal for Numerical Methods in Engineering*, 99(8):587–610.
- [Jiang et al., 2015] Jiang, C., Zhang, Z.-Q., Liu, G. R., Han, X., and Zeng, W. (2015). An edge-based/node-based selective smoothed finite element method using tetrahedrons for cardiovascular tissues. *Engineering Analysis with Boundary Elements*, 59:62–77.
- [Liu, 2019] Liu, G.-R. (2019). The smoothed finite element method (s-fem): A framework for the design of numerical models for desired solutions. *Frontiers of Structural and Civil Engineering*, 13(2):456–477.
- [Liu et al., 2007] Liu, G. R., Dai, K. Y., and Nguyen, T. T. (2007). A smoothed finite element method for mechanics problems. *Computational Mechanics*, 39(6):859–877.
- [Liu and Nguyen, 2010] Liu, G. R. and Nguyen, T. T. (2010). *Smoothed finite element methods*. CRC Press, 1st ed. edition.
- [Liu et al., 2009] Liu, G. R., Nguyen-Thoi, T., Nguyen-Xuan, H., and Lam, K. Y. (2009). A node-based smoothed finite element method (ns-fem) for upper bound solutions to solid mechanics problems. *Computers & Structures*, 87(1-2):14–26.
- [Martonova et al., 2021] Martonova, D., Alkassar, M., Seufert, J., Holz, D., Duong, M. T., Reischl, B., Friedrich, O., and Leyendecker, S. (2021).

- Passive mechanical properties in healthy and infarcted rat left ventricle characterised via a mixture model. *Journal of the Mechanical Behavior of Biomedical Materials*, 119:104430.
- [Martonová et al., 2021] Martonová, D., Holz, D., Duong, M. T., and Leyendecker, S. (2021). Towards the simulation of active cardiac mechanics using a smoothed finite element method. *Journal of biomechanics*, 115:110153.
- [Martonová et al., 2023] Martonová, D., Holz, D., Duong, M. T., and Leyendecker, S. (2023). Smoothed finite element methods in simulation of active contraction of myocardial tissue samples. *Journal of biomechanics*, 157:111691.
- [Mendizabal et al., 2017] Mendizabal, A., Bessard Duparc, R., Bui, H. P., Paulus, C. J., Peterlik, I., and Cotin, S. (2017). Face-based smoothed finite element method for real-time simulation of soft tissue. *Medical Imaging 2017: Image-Guided Procedures, Robotic Interventions, and Modeling*.
- [Minh Tuan Duong, 2014] Minh Tuan Duong (2014). *Hyperelastic Modeling and Soft-Tissue Growth Integrated with the Smoothed Finite Element Method-SFEM*. Dissertation, Rheinisch-Westfälische Technische Hochschule Aachen, Aachen.
- [Nash and Panfilov, 2004] Nash, M. P. and Panfilov, A. V. (2004). Electromechanical model of excitable tissue to study reentrant cardiac arrhythmias. *Progress in biophysics and molecular biology*, 85(2-3):501–522.
- [Nguyen-Thoi et al., 2009] Nguyen-Thoi, T., Liu, G. R., Lam, K. Y., and Zhang, G. Y. (2009). A face-based smoothed finite element method (fs-fem) for 3d linear and geometrically non-linear solid mechanics problems using 4-node tetrahedral elements. *International Journal for Numerical Methods in Engineering*, 78(3):324–353.
- [Nguyen-Thoi et al., 2010] Nguyen-Thoi, T., Vu-Do, H. C., Rabczuk, T., and Nguyen-Xuan, H. (2010). A node-based smoothed finite element method (ns-fem) for upper bound solution to visco-elastoplastic analyses of solids using triangular and tetrahedral meshes. *Computer Methods in Applied Mechanics and Engineering*, 199(45-48):3005–3027.
- [Townsend et al., 2022] Townsend, N., Kazakiewicz, D., Lucy Wright, F., Timmis, A., Huculeci, R., Torbica, A., Gale, C. P., Achenbach, S., Weidinger, F., and Vardas, P. (2022). Epidemiology of cardiovascular disease in europe. *Nature reviews. Cardiology*, 19(2):133–143.
- [Wang et al., 2015] Wang, G., Cui, X. Y., Feng, H., and Li, G. Y. (2015). A stable node-based smoothed finite element method for acoustic problems. *Computer Methods in Applied Mechanics and Engineering*, 297:348–370.

- [Wang et al., 2016] Wang, S., Decker, M., Henann, D. L., and Chester, S. A. (2016). Modeling of dielectric viscoelastomers with application to electromechanical instabilities. *Journal of the Mechanics and Physics of Solids*, 95:213–229.
- [World Health Organization, 2021] World Health Organization (2021). Cardiovascular diseases (cvds).
- [Wriggers, 2008] Wriggers, P. (2008). *Nonlinear Finite Element Methods*. Springer Berlin Heidelberg, Berlin, Heidelberg.
- [Zhao et al., 2007] Zhao, X., Hong, W., and Suo, Z. (2007). Electromechanical hysteresis and coexistent states in dielectric elastomers. *Physical Review B*, 76(13).
- [Zheng et al., 2019] Zheng, J., Duan, Z., and Zhou, L. (2019). A coupling electromechanical cell-based smoothed finite element method based on micromechanics for dynamic characteristics of piezoelectric composite materials. *Advances in Materials Science and Engineering*, 2019:1–16.